

Measurement of Condensed-Phase Reaction Kinetics in the Aerosol Phase Using Single Particle Mass Spectrometry

R. Mahadevan, D. Lee, H. Sakurai, and M. R. Zachariah*

Center for NanoEnergetics Research, Departments of Mechanical Engineering and Chemistry, University of Minnesota, Minneapolis, Minnesota 55455

Received: March 18, 2002; In Final Form: June 4, 2002

We applied a recently developed single particle mass spectrometer to analyze the elemental composition of individual aerosol particles and applied the technique to study the kinetics of thermal decomposition of metal nitrate aerosols (aluminum, calcium, silver, and strontium). Such decomposition processes on the industrial scale is known as spray pyrolysis and is a common method for making metal and metal oxide particles. Metal nitrate aerosols were passed through a tube furnace to induce thermal decomposition and transformation into oxides, and were delivered with high efficiency into the vacuum system of the single particle mass spectrometer using an aerodynamics lens arrangement. The particles were ablated and torn down to atomic ions with a tightly focused, high-power pulsed laser in the extraction field of the time-of-flight mass spectrometer. The mass spectra thus obtained are shown to carry a quantitative signature of the elemental composition of individual particles, and allow for on-line measurement of the stoichiometry transition from nitrate to oxide as the particles passed through a tube furnace. The results were used to calculate the reaction rates and activation energies for the decomposition reaction. In parallel, reaction rates were obtained by conventional thermogravimetric analysis, and a comparison revealed significant differences in measured reaction rates between the aerosol and conventional methods. In particular, it was found that the reaction rates determined in the aerosol phase were significantly higher than those obtained by traditional thermal methods, which we believe is associated with heat and mass transfer limitations associated with bulk methods. This new aerosol-based technique may offer an alternative approach to study condensed-phase reactions with minimal influence of artifacts caused by heat and mass transfer effects known to plague conventional thermal analyses.

I. Introduction

The basis of the work presented in this paper is directed to the development of a robust tool for measurement of chemical composition and reaction kinetics internal to aerosol particles. The primary motivation is directed toward the following two problems:

Aerosols play an important role as both a source of environmental/health impact, and as building blocks to advanced materials. In the latter case, aerosols are synthesized from either gas or liquid-phase precursors with the objective of producing particles with desired size (often submicrometers or smaller), morphology, and composition. Although on-line characterization of size is a well developed method, and morphology characterization based on light scattering has received considerable attention in the past decade, chemical composition determination is still in its infancy.¹ Many such materials are produced by spray-pyrolysis techniques in which liquid droplets containing precursors are injected into a thermal reactor, with resulting evaporation of solvent and reaction of the precursors to form product particles. To have better control in such industrial particle production processes, there is a need to understand aerosol-phase reaction kinetics that governs the final characteristics of product particles.²

The measurement of condensed-phase reaction kinetics is usually performed using conventional dynamic thermal tech-

niques such as thermogravimetry (TG). Despite the fact that over 90% of solid-state reactions have been studied in this manner, there is still considerable controversy regarding the reliability of these methods.³ The literature is rife with examples indicating that traditional thermal analysis is plagued by experimental uncertainties associated with heat and mass transfer effects, which results in kinetic parameters that are dependent on experimental artifacts.^{3,4} Aerosol-based techniques, which resemble the infrastructure and methods used by gas-phase kineticists, have advantage of minimal sample size and presumably minimal artifacts due to mass/heat transfer effects, and therefore may provide an additional and complimentary method for characterization of condensed-phase reaction kinetics.

We recently developed a single-particle mass spectrometer (SPMS) which is capable of carrying out quantitative measurements of reaction kinetics internal to aerosol particles. The most crucial feature of the mass spectrometer is the capability of determining the elemental composition of individual particles in a quantitative manner. This is accomplished by using a tightly focused, high-power pulsed laser for ablation and ionization of particles, in a manner analogous to that demonstrated by Reents et al.^{5–7} Although no molecular information of particles can be retrieved, this technique allows us to determine quantitatively the elemental stoichiometry of each particle, by having near-unity efficiencies for both particle dissociation into constituent atoms and their ionization. In addition, our mass spectrometer is equipped with an aerodynamic lens inlet, as was done in the system developed by Kane et al.⁸ The aerodynamic lens inlet

* To whom correspondence should be addressed. Michael R. Zachariah, University of Minnesota, 111 Church St. S. E., Minneapolis, MN 55345. E-mail: mrz@me.umn.edu. Fax: 612-625-6069.

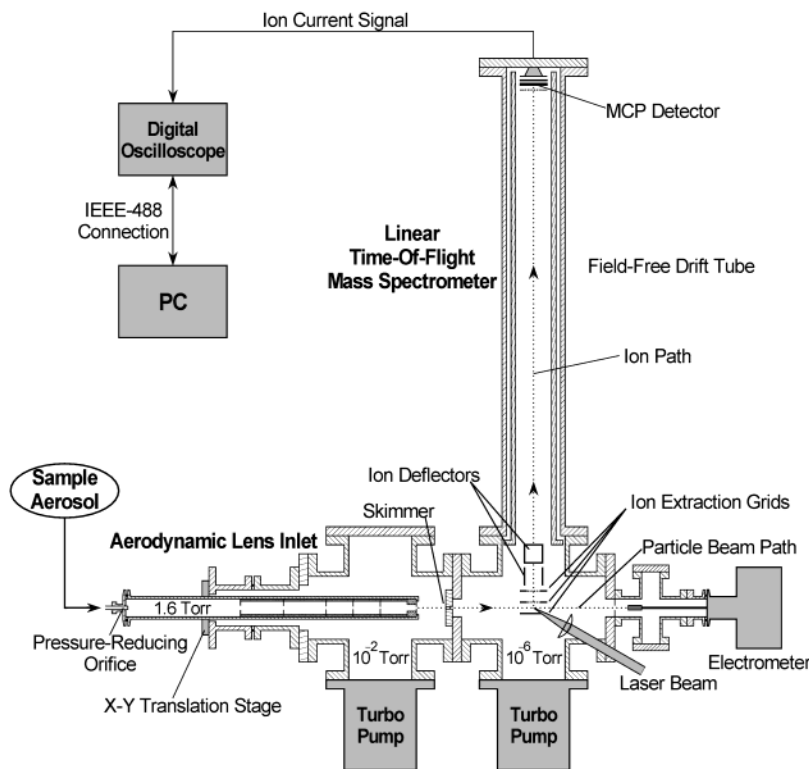


Figure 1. Schematic of the linear time-of-flight single particle mass spectrometer (SPMS).

provided a method for formation of a very narrow, collimated particle beam in a vacuum and efficient transmission of particles through differential pumping stages. The tightly collimated particle beam significantly increases the probability for particles to be hit by the tightly focused laser beam. Design of the mass spectrometer and results from a series of characterization experiments are presented in sections II and III, respectively.

Section IV describes results of our reaction kinetics measurement on a spray-pyrolysis process using the SPMS technique. We chose metal nitrates (aluminum, calcium, silver, and strontium) for the study, as they are the primary precursors used in the production of metal-oxides by spray-pyrolysis methods. We determined the reaction rates of the decomposition process of the nitrates at different temperatures, and applied a first-order reaction kinetics model to calculate the reaction rate constants as well as the activation energy and preexponential factor of the Arrhenius equation. Also in section IV, we report results of thermogravimetric analysis for thermal decomposition of calcium nitrate. There, it was confirmed that the sample mass acts as an artifact; the reaction rates determined by this conventional technique varied when the sample mass used was changed. In addition, comparison of these results with our SPMS results is made, in which the reaction rates determined by the SPMS technique were found to be significantly higher than those determined by the TG method. Possible reasons for the difference in the measured reaction rates are briefly discussed.

II. Experimental Section

A. Single-Particle Mass Spectrometer (SPMS). A schematic diagram of the single-particle mass spectrometer (SPMS) used in this study is shown in Figure 1. The primary components of this system consisted of an aerodynamic lens inlet, two-stage differential pumping system, free-firing dissociation/ionization laser and optics system, linear time-of-flight mass spectrometer, and data acquisition system composed of a fast, digital storage oscilloscope and a PC. The aerodynamic lens inlet used in this

system was similar to the one developed by Liu et al.^{9–10} Its purpose, through the use of a series of contractions (lenses), is to produce a narrow collimated beam of particles that can be injected with high transport efficiency into high vacuum. Components in the inlet are, from upstream to downstream, a pressurereducing orifice of ~ 0.1 mm diameter opening, a series of aerodynamic lenses made of thin-plate orifices with opening diameters of 8, 7, 6, 5, and 4 mm, an accelerating nozzle of 6-mm diameter, and a thin-plate final orifice of 3 mm diameter. After the pressurereducing orifice, there was a 240-mm long flow relaxation section before the first aerodynamic lens orifice. The aerodynamic lenses were separated with spacer tubes of 25 mm i.d. of either 50 or 80 mm in length. The accelerating nozzle was 10 mm long. All of the above components were housed in a stainless steel tube of 36 mm i.d. and 560 mm long. The pressure in this inlet tube after the pressurereducing orifice was 1.6 Torr when the pressure upstream of the inlet was maintained at 1 atm, whereas the pressure in the first stage vacuum chamber, which was pumped by a 250 L/sec turbo molecular pump, was $\sim 10^{-2}$ Torr. The second stage was pumped with another 250 L/sec turbo pump and its pressure was $\sim 10^{-6}$ Torr when the mass spectrometer inlet was open. Downstream of the exit of the aerodynamic lens inlet, there was a skimmer of 3-mm circular opening and 25-mm long at the distance of 65 mm, which separated the first and second differential pumping stages. The center of the extraction field of the time-of-flight mass spectrometer, placed in the second pumping stage, was located 140 mm downstream of the inlet end. Positioning of the aerodynamic lens inlet was adjusted with an X–Y translation stage mounted on a vacuum flange of the first-stage vacuum chamber. Alignment of the inlet tube with respect to the skimmer hole was accomplished with the X–Y translation stage by feeding charged particles into the vacuum system through the inlet, and maximizing the particle current detected with a Faraday cup detector connected to an electrometer which was located downstream of the extraction region of

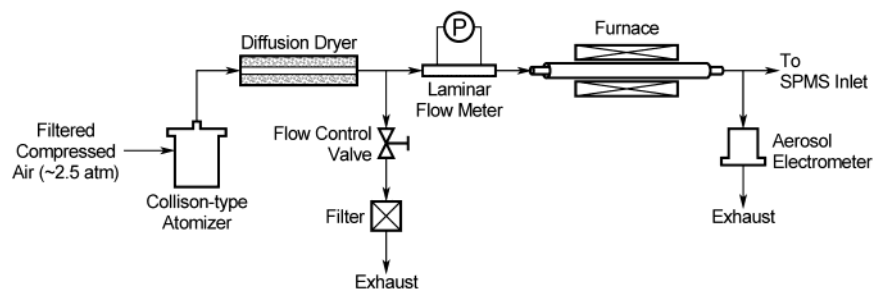


Figure 2. Schematic of the aerosol generator and thermal reactor system.

the time-of-flight mass spectrometer while no voltage was applied to the extraction grids.

The laser used in this system was a frequency-doubled Nd:YAG operated at 10 Hz in the internal Q-switch mode. Two dichroic mirrors were used to separate the 532 nm light from the fundamental infrared. The laser energy measured before the laser entrance window of the mass spectrometer was about 60 mJ/pulse. A spherical plano-convex lens with the focal length of 38 mm and the f-number of 1.5 was mounted inside the vacuum chamber to focus the laser beam tightly at the center of the extraction field of the mass spectrometer. The lens itself had no position adjustment mechanism, and the fine alignment of the laser beam position with respect to the particle beam was done by adjusting two mirrors which were located outside of the vacuum chamber. The laser power density at the focal point was estimated to be approximately 1.7×10^{10} W/cm² assuming the beam diameter at the focal point be 0.3 mm and the laser pulse duration of 5 ns. The beam diameter at the focus is at best a reasonable guess. The diffraction limited spot size assuming a Gaussian beam profile would be but a few microns, whereas on the other extreme spherical aberration would give a spot size of 0.75 microns. Our estimate of 300 microns is based on a visual observation taken with a CCD camera of the plasma ball generated at the outlet of a capillary tube flowing air. As such, the assumption of 0.3 mm is an upper estimate. On a practical note, the latter point is probably mute since only a small fraction of particle would actually intersect the exact focal point. Each laser shot was detected with a photodiode sensor to initiate the time-of-flight measurement in the data acquisition system.

Because the laser was operated in the free fire mode, we rely on the chance encounter between the beam and particle. When the laser beam intercepts a particle, atomic ions comprising the particle are generated in the extraction electric field of the mass spectrometer. Only positive ions, which had either one or multiple elemental charges, were accelerated along the 1-m long linear time-of-flight tube and were detected by Z-stuck micro-channel plates. Voltages of 0, 3350, and 4500 V were applied to the top, middle, and bottom electrodes of the ion extraction electrode assembly, respectively. The distances of the top-middle and middle-bottom gaps were both 1.2 cm, which gave the electric field strength of about 960 V/cm at the ion source spot. The ion signal was stored as a time-of-flight spectrum in a 500-MHz digital storage oscilloscope which was capable of selectively recording spectra of only "successful" particle hits. A "successful" particle hit was defined as an event in which the intensity of ion signal for any mass-to-charge ratio exceeded a certain level set on the oscilloscope. Time-of-flight spectra thus obtained were analyzed either on the oscilloscope or on a PC.

B. Generation of Metal Nitrate Aerosols. Figure 2 shows the apparatus used in front of the SPMS to generate and process metal nitrate aerosols, which is essentially the same as that used

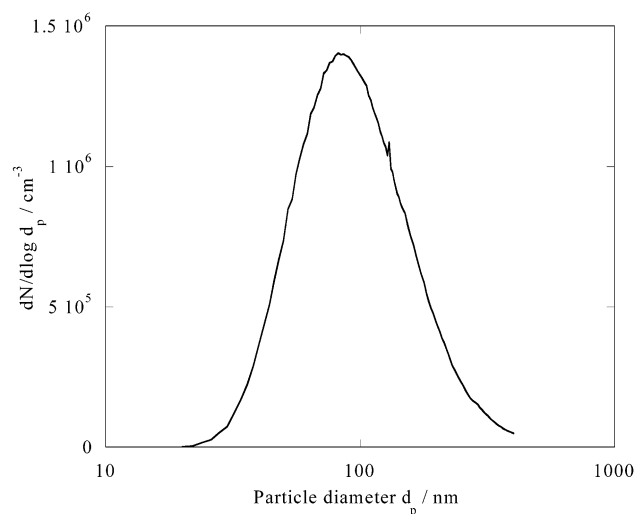


Figure 3. Number-weighted size distribution of sodium chloride particles generated from a 1-wt % solution.

for production of particles by spray pyrolysis.² A solution of nitrate, typically of 1 wt %, was prepared by mixing commercially available metal nitrates (> 99% in purity) with filtered deionized water which was then atomized in air to generate aerosol droplets of the solution. The droplet-laden air was then passed through an aerosol dryer filled with dry silica gel to remove most of water content in the droplets, and delivered to a heated flow tube. The heated flow tube was made of stainless steel with 1.0 cm i.d., and 120 cm long, and was suspended in a 2.5 cm i.d. alumina tube placed in a tube furnace, with a heated length of 30 cm. A more extensive discussion of temperature measurement within the reactor can be found in ref 11. This arrangement eliminated hot spots in the stainless steel tube, which could be caused by uneven furnace heating elements or by contact between the alumina and the stainless steel tubes.¹¹ The aerosol flow rate from the atomizer was about 2 L/min, and the flow rate in the heated flow-tube was monitored with a laminar flow meter in front of the furnace, and was adjusted to 1.0 L/min at ambient pressure and temperature by controlling the flow rate to the excess flow path split before the laminar flow meter. The output aerosol from the furnace was split into two, one which was delivered to the SPMS, and the other was used for monitoring the aerosol concentration with an aerosol electrometer.

Figure 3 shows the size distribution of sodium chloride aerosol particles generated with a 1-wt % solution exiting the atomizer and dryer, as determined by a homemade differential mobility analyzer and a condensation particle counter. The measured size distribution fits quite well to a log-normal distribution with the geometric mean diameter and standard deviation of 93 nm and 1.29, respectively, and with a total concentration of about 8×10^5 particles/cm³.

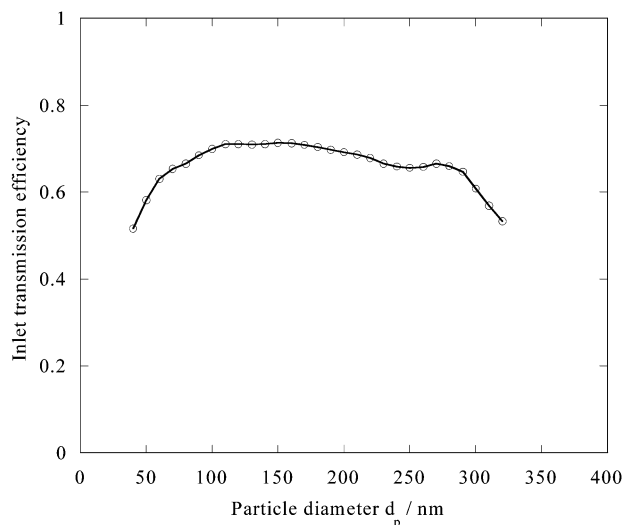


Figure 4. Particle transmission efficiency through the aerodynamic lens inlet and differential pumping system.

III. Characterization of SPMS

A. Particle Transmission Efficiency and Laser Hit Rate.

The transmission efficiency of aerosol particles through the aerodynamic lens inlet and the skimmer in the SPMS was determined experimentally. Monodispersed dioctyl sebacate (DOS) particles of known sizes were generated by aerosolization, followed by size selection with a differential mobility analyzer (DMA). The aerosol current (number of particles per unit time) flowing into the pressurereducing orifice was estimated from the particle concentration measured by the aerosol electrometer (see Figure 2) and the volume flow rate through the orifice. The aerosol current after the skimmer was measured with the Faraday cup as shown in Figure 1. The result is presented in Figure 4. Efficiencies greater than 60% were observed in the size range between 50 and 300 nm. Liu et al. reported transmission efficiencies in excess of 90% through their aerodynamic lens inlet for particles of 30–250 nm¹⁰. The reduced efficiency for the SPMS inlet could be due to a broader beam diameter caused by slight misalignment of aerodynamic lens components and consequent beam blockage by the skimmer wall. It should be noted that the uncertainties in measured transmission efficiencies were larger at both ends of the transmission curve. This was due to the lower concentrations of aerosols sampled at the high and low ends. Uncertainties were roughly 5% at 100 nm, and up to 50% at 50 and 300 nm.

Kane et al. reported that the particle detection efficiency of their single-particle mass spectrometer was dependent on the particle size, and introduced a formula of the particle hit rate which was defined as the number of particles per unit time that were hit by the laser beam “successfully”, as

$$\text{ParticleHitRate} = n_{\text{aerosol}} \cdot V \cdot T \cdot \frac{A_L}{A_p} \cdot L \cdot E_{\text{ablation}}$$

where n_{aerosol} is the number concentration of sample aerosol before the mass spectrometer inlet, V is the volume flow rate through the inlet, T is the transmission efficiency through the inlet and differential pumping stages, A_L/A_p is the ratio of the cross sectional area of the laser beam to that of the particle beam, L is the laser duty factor which is defined as the particle transit time through the laser beam multiplied by the laser repetition rate, and E_{ablation} is the ablation efficiency which is the fraction of particles ablated in the laser beam which produce

sufficient number of ions to be deducted.⁸ We determined the particle hit rate by using the sodium chloride aerosol in Figure 3 without size selection. The particle number concentration and volume flow rate before the inlet were 10⁶ particles/cm³ and 1 cm³/s, respectively. The inlet transmission efficiency of 70% was obtained from the data in Figure 4 for 90-nm particles. The laser and particle diameters were assumed to be 0.3 mm and 0.5 mm (the Brownian-limit diameter based on the calculation method by Liu et al.⁸), respectively. The laser duty factor was calculated using the laser beam diameter of 0.3 mm, particle beam velocity of 170 m/sec, and the laser repetition rate of 10 Hz. If the ablation efficiency is assumed to be 100%, the hit rate is calculated to be ~4.4 particles/sec. On the other hand, the observed hit rate was 0.33 particles/sec under this condition, which gives an ablation efficiency of ~7%. Because we expect that any particles in the focal volume of the laser beam would generate measurable ion signal at such a high laser power density, we think this low ablation efficiency is due to the size of the particle beam being broader than that estimated and/or misalignment between the laser and particle beams.

B. Quantitative Determination of the Elemental Stoichiometry of Aerosol Particles.

To obtain any meaningful kinetic results, we needed to determine the accuracy with which one can measure elemental composition. For this, we sampled laboratory-generated aerosols of known elemental stoichiometry into the SPMS. Figure 5 shows examples of typical particle mass spectra obtained for an individual particle (a) for sodium chloride, (b) for aluminum nitrate, and (c) for aluminum oxide. The sodium chloride and aluminum nitrate spectra were obtained with aerosols generated in the same method as described in the Experimental Section, with the furnace turned off. Aluminum oxide particles were generated in the same setup by heating the furnace to 800 °C. Because of the aggressive nature of the ablation/ionization process, no multi-atomic species were observed in any spectra, and multiply charged atomic ion peaks were present in many spectra. The latter observation implies the laser beam intensity was extremely high and both dissociation and ionization were very efficient. For example the energy needed to vaporize and ionize all the atoms in a 100 nm particle is about 0.04 pJ, whereas the photon energy hitting the particle a spherical 100 nm particle with our laser (at the focal point) is roughly 60 nJ. In Figure 5(a), we see that the atomic hydrogen and oxygen peaks exhibited high intensity. This indicates that there was a substantial water remaining in this sodium chloride particle. Similarly, Figure 5(b) exhibits hydrogen and oxygen peaks. This is not surprising because, despite the drying process, both NaCl and the nitrate are hygroscopic materials and the occurrence of the hydrogen we attribute to water. In the case of nitrate, however, the oxygen peaks are attributed to both water and the nitrate. Indeed, for such cases, the oxygen contribution from the nitrate is calculated by first estimating the oxygen ion contribution from water using the hydrogen ion signal, and then subtracting it from the total oxygen ion intensity.

We assumed the peak area for an ion of any given mass-to-charge ratio was proportional to the number of ions of the same m/z that were generated at the ion source of the mass spectrometer. In addition, we also assumed complete dissociation and ionization of a particle by irradiation of an extremely intense laser beam, and therefore the number of atoms of a certain element in a given particle must be proportional to the sum of the peak areas of ions (singly and multiply charged) of the same element. Thus, the elemental stoichiometry of any pair of elements in a given single particle can be estimated as the ratio of the sum of peak areas of one element to that of the other.

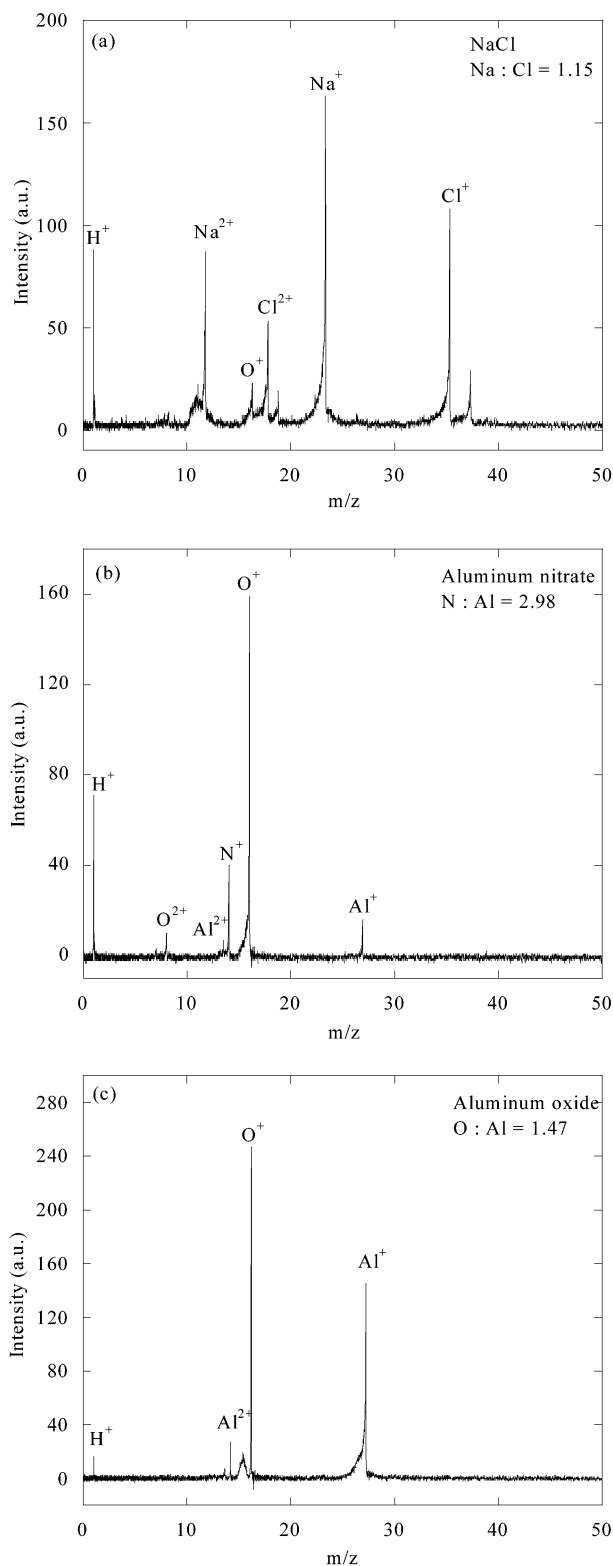


Figure 5. Single particle mass spectra for (a) sodium chloride, (b) aluminum nitrate and (c) aluminum oxide. The elemental stoichiometry ratio for these example spectra are indicated on each plot.

For the particles in Figure 5, the elemental stoichiometry of Na/Cl for sodium chloride, N/Al for aluminum nitrate, and O/Al for aluminum oxide were 1.15, 2.98, 1.47, respectively. These values agree very well with the theoretical values, i.e., 1.00, 3.00, and 1.50 for Na/Cl, N/Al, and O/Al, respectively.

To evaluate the uncertainty of the stoichiometry measurement, a number of individual particle mass spectra of known compositions were analyzed by SPMS, to obtain a probability distribu-

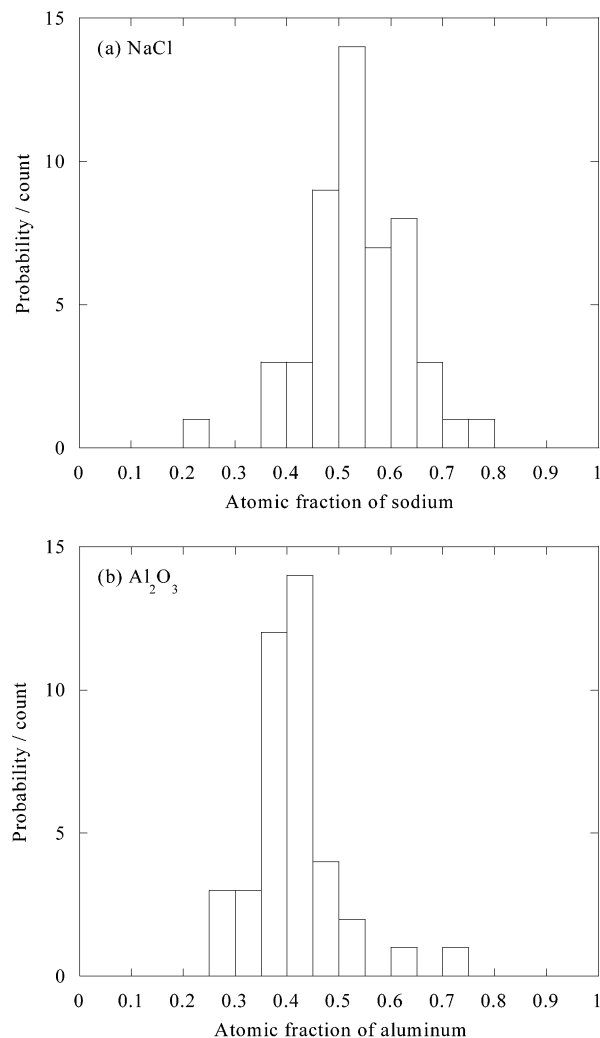


Figure 6. Histograms for the shot-to-shot elemental stoichiometry obtained by SPMS from (a) 50 NaCl and (b) 40 Al₂O₃ particles.

tion of measured stoichiometry ratios. Figure 6(a) and (b) presents the results for 50 sodium chloride and 40 aluminum oxide particles, respectively. The mode of the distribution of the atomic sodium fraction for NaCl particles was located at the bin of 0.50–0.55 and was close to the expected theoretical value of 0.50. About 66% of the particles exhibited the sodium fraction which was within 20% of the theoretical value. In the case of aluminum oxide, the mode of the distribution of the atomic aluminum fraction was about 0.4 and matched well with the theoretical stoichiometry. About 80% of particles had the aluminum fraction within 20% of the theoretical value, which was better than the case of sodium chloride. It should be noted that the experiment with sodium chloride is potentially one of the most challenging for determination of elemental stoichiometry, because of large difference in the ionization potential and electron affinity between the two elements. The ionization potential of sodium and chlorine are 5.1 and 13.0 eV, respectively, and the electron affinity are 0.55 and 3.6 eV, respectively. These thermodynamic values imply that the most probable charging state, in the case that ions are formed after dissociation of a pair of sodium and chlorine atoms, would be Na⁺ and Cl⁻, and that photon energy of as much as 17 eV must be put into the chlorine anion after the dissociation, to remove two electrons and form Cl⁺. Therefore, we might expect the measured sodium fraction to be greater than that of chlorine unless a sufficient amount of energy was applied to the particle and could be

TABLE 1: Stoichiometry Ratios Obtained by SPMS for Various Aerosols and Comparison with Theoretical Values

particle	ratio considered	experimental value	theoretical value	% error
aluminum nitrate	N: Al	3.08	3.00	2.7
aluminum oxide	O: Al	1.47	1.50	-2.0
sodium chloride	Na: Cl	1.14	1.00	14.0
	³⁵ Cl: ³⁷ Cl	3.00	3.13	-4.2
strontium nitrate	N: Sr	1.95	2.00	-2.5
silver	¹⁰⁷ Ag: ¹⁰⁹ Ag	1.12	1.08	3.7
silver nitrate	N: Ag	0.98	1.00	-2.0
iron nitrate	N: Fe	2.86	3.00	-4.7
ammonium sulfate	N: S	2.27	2.00	13.5

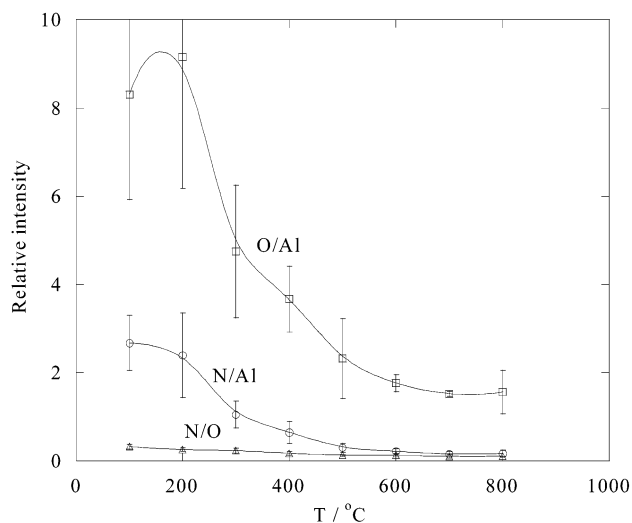
efficiently coupled to the resulting plasma. Knowing that the laser power density had a spatial distribution around the tight focal spot, and also that a slight shot-to-shot variation in the laser power would give a significant difference in this highly nonlinear, multiphoton breakdown processes, the fact that the observed shift of the sodium fraction curve is only slightly above 0.5 is quite remarkable, and provided confidence that the laser power used in this study should be sufficient for a wide range of compounds. We should point out that the width of the sodium chloride probability distribution found in the study by Reents and Schabel⁶ was narrower than that in this study, which we believe is associated with the differences in the nature of the sample introduction and its impact on the resulting spatial width of the particle beam. Reents-Schabel introduces particles using a capillary inlet, which while reducing particle transmission efficiency, also allows them to ablate/ionize just at exit of the capillary, where the particle beam is narrowest. We speculate that with the Reents approach a larger fraction of the particles are intercepted by the most intense part of the laser beam. As a method to classify a single particle mass spectrum based on the laser energy applied the particle, Reents and Schabel also suggested that the ratio of the doubly charged ion intensity to that of the corresponding singly charged ion could be used as an indicator of complete ionization, and that it should exceed 10% for the mass spectrum to be classified as “successful”.⁶ We adopted the same criterion whereby spectra containing less than 10% doubly ionized peaks were discarded.

Table 1 summarizes the elemental stoichiometry ratios of several laboratory-generated aerosols. The ratios were obtained from mass spectra which were obtained by averaging 20–50 “successful” single particle spectra for each material. The measured and theoretical values showed good agreement, and provides the basis from which we believe we can conduct quantitative elemental evaluations which could be used to assess changes due to chemical reactions within aerosol particles. The largest error was observed for sodium chloride (14%), which we think is reasonable based on the discussion presented above regarding the difference in the ionization potential and electron affinity between the two elements.

IV. Results and Discussion

A. Condensed-Phase Reaction Kinetics Study by SPMS.

To generate kinetic data, we introduced metal nitrate aerosol to the tube furnace for a fixed residence time (~1 s) and conducted elemental composition analysis with the SPMS for various furnace temperature conditions. Figure 7 shows the stoichiometry ratios of O/Al, N/Al, and N/O for decomposition of aluminum nitrate at varied temperatures in the spray pyrolysis setup shown in Figure 2. At 100 °C, the ratio of nitrogen to aluminum is about 2.7 (expected stoichiometry of 3:1), whereas oxygen-to-aluminum ratio was ~8.3, and reflect that reactant

**Figure 7.** Relative intensities of nitrogen, oxygen, and aluminum ion peaks during thermal decomposition of aluminum nitrate.

particles are just starting to decompose. For calculation of the O/Al and N/O ratios at low temperatures, the oxygen contribution due to the presence of water, which was described earlier, was taken into account. Reduction of the nitrogen fraction, found in both N/Al and N/O, revealed progress of nitrate decomposition at higher temperatures. At 800 °C, the reaction was effective completed, and the O/Al ratio reaching a value of ~1.5, which corresponds to the theoretical stoichiometry of aluminum oxide, whereas the nitrogen fraction reached a negligible small value. It should be noted that, for a given temperature condition, some mass spectra which were classified “successful” according to the criterion described in the previous section were found to have very different stoichiometry compared to others at the same temperature. More specifically, some mass spectra showed particles had not reacted much, whereas some others were found to have completely decomposed to oxide. This effect is reflected in the uncertainty bars shown for the data in Figure 7. This behavior is a combination of the inherent limitations of the instrument as presented in the previous section, as well as differences in the heating history of particles in a tubular reactor. In the latter case, since the flow in the heated reactor is laminar, and particles have low diffusivities, those particles which entered the reactor near the center line stayed in the reactor for about a half the average residence time, while those traveled near the tube wall spent significantly longer time in the heated tube. We should point out that we have measured and estimated radial temperature gradients and radiation heating effects which might compromise the accuracy of the results, and have found these effect to be negligible. A more thorough discussion of the effects of residence time distribution, radial and radiation temperature effect have been addressed in a very recent work of ours that studied the oxidation of size selected soot nanoparticles.¹¹ The uncertainty in the measured reactivity was most pronounced when the temperature was near the onset of the decomposition reaction, and we excluded those extremes from the stoichiometry ratio determination. The error bars in Figure 7 represents the standard deviations, which were greater for lower temperatures. As an example, about 30% of mass spectra were initially discarded from the data set obtained at 200 °C, after which the remaining were checked for “successful” laser shots.

To evaluate the reaction rate we define in the usual way the extent of conversion, $\alpha \equiv (w_0 - w)/(w_0 - w_f)$, where w is the sample mass and the subscripts 0 and f represent the initial and final states of the reaction, respectively. α could then be

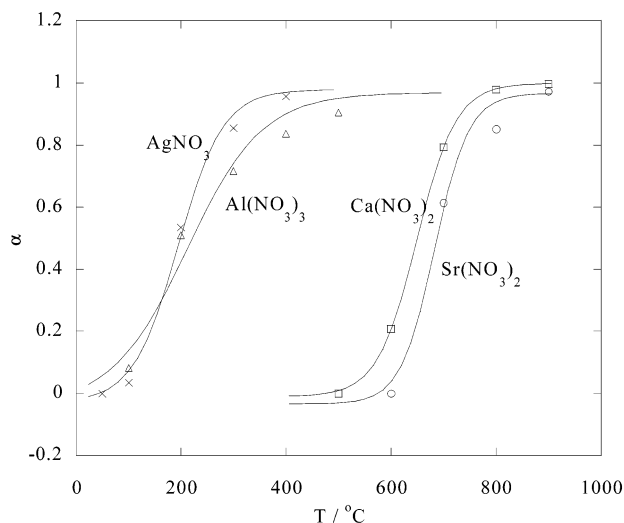


Figure 8. Temperature dependence of the extent of conversion obtained by SPMS for four metal nitrates.

calculated using any of the following relationships

$$\alpha = 1 - [N/Al]/3 \text{ with } N/Al$$

$$\alpha = (18 - 2[O/Al])/15 \text{ with } O/Al, \text{ or}$$

$$\alpha = (3 - [O/N])/(5/2 - [O/N]) \text{ with } O/N$$

Note the first expression of the extent of conversion does not use the oxygen ion peak intensity. This could be important because the analysis of the nitrate decomposition by SPMS would not suffer from complications arising from the presence of remaining water in particles. However, we found the extents of conversion calculated for a single mass spectrum with the above equations gave different values. We instead used a method which used two of the atomic ratios, N/Al and O/N, to calculate the extent of conversion. That is, we considered the atomic fraction of nitrogen in particles, $\langle N \rangle$ from

$$\langle N \rangle = \frac{N}{Al + N + O} = \frac{1}{[Al/N] + 1 + [O/N]}$$

This expression is evaluated by substituting for $[Al/N]$ and $[O/N]$ from the ratio peak areas obtained from the mass spectra. At the same time, from the relationship between α and the atomic ratios in the equations above, the extent of conversion can be obtained from the atomic fraction. Overall, the relationship between α and $\langle N \rangle$ can be expressed as

$$\alpha = \frac{(13/3)\langle N \rangle - 1}{(7/2)\langle N \rangle - 1}$$

Figure 8 shows plots of the extents of conversion for four metal nitrates (aluminum, calcium, silver, and strontium) at different reaction temperatures. Silver and aluminum nitrates exhibited lower decomposition temperatures (~ 200 °C for $\alpha = 0.5$) whereas 50% conversion was observed for calcium and strontium nitrates at temperatures above 650 °C. It should be pointed out that the temperatures at which the decomposition reaction took place in SPMS was at or above the melting point of the nitrates; the melting point of aluminum, calcium, silver, and strontium nitrate are 73, 561, 212, and 570 °C, respectively.¹² This means the decomposition occurred in the molten phase in our SPMS study.

The reaction rate constant, $k(T)$, was calculated by using the extent of conversion and assumed that the overall reaction

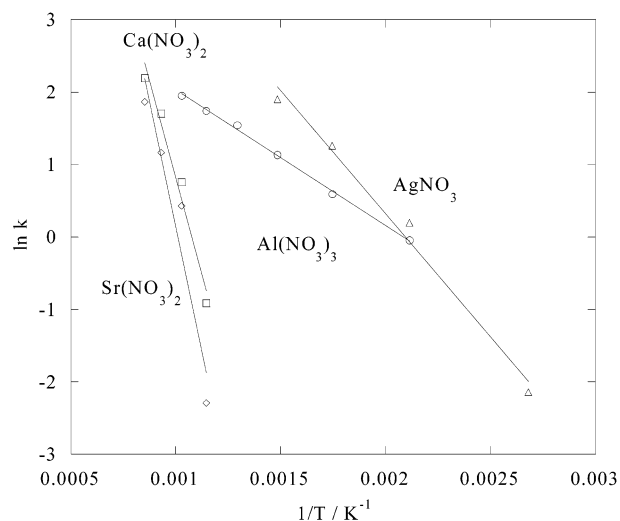


Figure 9. Arrhenius plot for thermal decomposition of metal nitrates obtained by SPMS.

TABLE 2: Arrhenius Parameters Obtained by SPMS for Thermal Decomposition of Various Metal Nitrates

	E [kJ/mol]	$\ln A$ [ln sec ⁻¹]
Sr(NO ₃) ₂	115.3 ± 23.1	14.1 ± 2.8
Ca(NO ₃) ₂	89.1 ± 10.5	11.5 ± 1.3
Al(NO ₃) ₃	15.6 ± 0.4	3.9 ± 0.1
AgNO ₃	28.3 ± 2.3	7.1 ± 0.6

obeyed a first-order rate law. Equation A3 in Appendix shows the relationship between α , $k(T)$, and the Arrhenius parameters, (activation energy (E) and preexponential factor (A)). Results for the computed rate constant $k(T)$ are shown in Figure 9. Each nitrate exhibited good linearity on a semilog plot which implies that the single-step first-order assumption, and use of the Arrhenius relationship are reasonable. Table 2 tabulates the fitted Arrhenius parameters obtained.

B. Kinetics Analysis by Thermogravimetry and Comparison with SPMS Results. In an effort to put our rate data measurements in perspective, we present a comparison with a reaction measurement conducted using standard thermogravimetric methods. A series of traditional, nonisothermal thermogravimetric measurements were conducted on calcium nitrate to compare the kinetics information obtained by this technique to that by SPMS. We chose calcium nitrate because it has been previously studied by Ettarh and Galwey by a thermal technique¹³ and we referred to it comparison with our results. In our thermogravimetric study, the initial sample mass and heating rate were varied as experimental parameters in a 20 cm³/min flow of dry air. We paid special attention to control the water content in the sample since calcium nitrate is hygroscopic. The original calcium nitrate powder was ground with a mortar and pestle to prepare fine powder, and stored for a several days at ambient temperature and 60%RH.

Figure 10 shows the thermograms that were obtained with different initial sample masses, which ranged from 1.33 to 21.39 mg for a heating rate of 10 °C/min. The initial weight loss, as much as 32% of the initial mass, that occurred in the temperature range from room temperature up to 200 °C was probably associated with loss of water in the samples. The second drop observed to start at about 500 °C, was due to thermal decomposition of the nitrate and the release of NO and NO₂ to the gas phase. The extent of conversion, α , was evaluated across this second drop region, and therefore does not include the weight loss below 200 °C. The melting point of calcium nitrate is 561 °C, which falls in the temperature range where the second

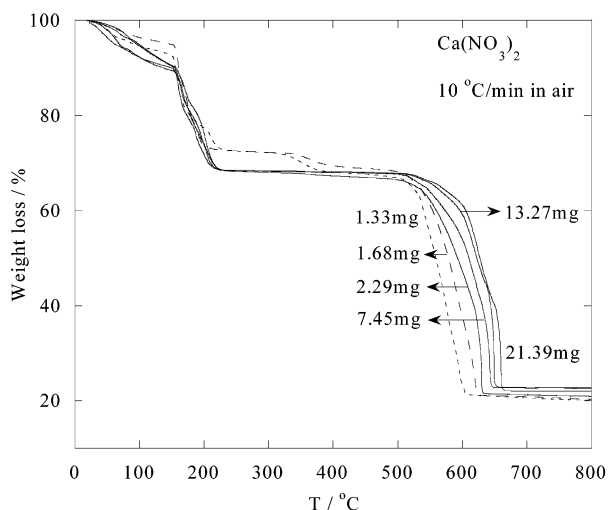


Figure 10. Weight loss profiles for thermal decomposition of calcium nitrate at a constant heating rate of 10 °C/min with different initial sample masses obtained by conventional nonisothermal TGA.

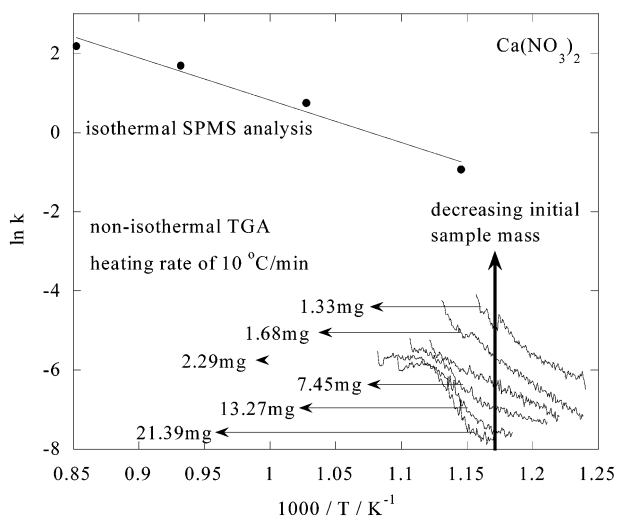


Figure 11. Comparison of the reaction rates of calcium nitrate obtained by SPMS and by conventional TGA.

drop was observed, indicating that a phase change is also likely occurring. Quite obvious in the figure is the effect of sample mass and the fact that the decomposition curve shifts to lower temperature as the initial sample mass was decreased. In other words, an increase in the sample size resulted in a decrease in the apparent reaction rate for a given temperature.

In Figure 11, we compare the kinetic measurements made by the two techniques in Arrhenius plots. The reaction rate constants for the TGA results were evaluated from eq A4 using the data in Figure 10, over the range in the extent of conversion from 0.1 to 0.9. We call attention to the fact that the temperature ranges over which the rate constants were obtained by the two techniques unfortunately do not overlap. This is because there was a significant difference in the dynamic range for a reaction rate measurement for a given temperature between the two techniques. The increase of the apparent reaction rate in TGA for decreasing mass is clearly demonstrated in this figure. It is interesting to note the reaction rate constant obtained from TGA moves up toward that of SPMS as the sample size used gets smaller. However, even with the smallest sample mass used in TGA (1.33 mg), there was a significant gap between TGA and SPMS, and the difference was approximately an order of magnitude at 600 °C. The initial sample size also affected the

shape of the temperature dependence in the Arrhenius plot. For example, the Arrhenius plot is linear for the cases where the initial sample masses were smaller than 2.29 mg. This indicates that the reaction model (single-step first-order) and Arrhenius relationship worked quite well altogether for this reaction system. On the other hand, the Arrhenius curve had a nonlinear structure when the initial sample mass was 7.45 mg or greater, and the same processing technique appeared to have failed. This is another example of the initial mass effect that plagues reaction kinetics study with TGA.

Discrimination of the causes of mass-loading on the observed kinetics in TGA is very difficult if not impossible to assess. The variety of potential mass-loading effects can range from simple heat capacity effects resulting in different actual heating rates for different sample sizes, to more complex phenomena. These might include longer diffusion paths for products of reaction for bulk samples. In the case of interest here, these might be evolution of NO or NO₂, where the observed kinetics would result from a slower mass loss rate, or the fact that the lowered loss rate of the NO_x results in a shift in the equilibrium constant as discussed by Ettarh and Galwey. Other effects might include different rates of melting as a function of sample size. In general, however, the observed increase in the apparent rate constant as the sample size decreases, implies that in the limit of very small sample sizes, we should be observing rate behavior that is uncorrupted by these other transport related effects.

At this point we note that the sample mass used for the SPMS evaluation was ~1 fg!!

Ultimately, the small size limit should be approached by a sample that is sufficiently small so as to minimize length scale effects associated with transport phenomena, but not so small as to introduce other length scale effects associated with nanoscaled materials. In the latter case, we know, for example, that the internal pressure of nanoparticles can be significantly above those of bulk. However, for particles in the 100–200 nm range the expected pressure is under 10 bar and is not sufficient to alter the reaction equilibrium constant significantly.¹⁷ The Kelvin effect is also relatively unimportant for particles above 100 nm in diameter and the melting point depression known for nanoparticles is usually only important for particles under 20 nm.¹ We feel confident therefore that our chemistry is not affected by any new phenomena that occurs at the nanoscale.

Finally, we carried out further experiments to determine the activation energy of calcium nitrate decomposition by the iso-conversional analysis employed in eq (A7). A small sample mass (1.6 ± 0.1 mg), which gave the best linearity in the Arrhenius plot in Figure 10, was heated at three different heating rates, i.e., 2.5, 5, and 10 °C/min. The activation energy by this analytical technique is known to differ with the extent of conversion used for calculation, and ranged from 220 to 300 kJ mol⁻¹ for the range of the extent of conversion between 0.25 and 0.9 in our case. In comparison, Ettarh and Galwey used an isothermal titration technique to study decomposition of calcium nitrate and reported that the reaction was described with two activation energies for different regimes of the extent of conversion, which are 217 ± 9 kJ mol⁻¹ for 0.3 < α < 0.6, and 298 ± 8 kJ mol⁻¹ for 0.7 < α < 0.9. Our activation energies by TGA are in reasonably agreement with those of Ettarh and Galwey, but is significantly different from the SPMS. In the previous section, we estimated the SPMS activation energy as 89.1 ± 10.5 kJ mol⁻¹. We are quite confident that given the accuracy with which we can measure elemental composition, that the difference in activation energies can either be attributable

to the fact that the two techniques worked at different temperature ranges, or more likely, given the demonstrated artifacts caused by the mass/heat transfer problems in TGA measurements, that the TGA is measuring a composite kinetic process.

V. Conclusions

We have developed a single-particle mass spectrometer (SPMS) and applied it to quantitative measurement of condensed-phase reaction kinetics. With the capability of the mass spectrometer for determining the elemental stoichiometry internal to individual aerosol particles, kinetics of thermal decomposition of various metal nitrate aerosols were studied, and the rate constants at different temperatures were fit to an Arrhenius expression. In parallel, we conducted traditional thermogravimetric analysis (TGA) of a nitrate to compare the results. The reaction rate observed in aerosol particles by SPMS was found to be significantly greater than that observed in TGA. We also confirmed that the sample mass used in TGA measurements greatly effects the reaction rate determined by this method. The difference in the reaction rate between SPMS and TGA, and the effect of the initial TGA sample size we attributed to the well-known artifacts inherent in the usage of conventional thermal methods for reaction kinetics studies. The new aerosol-based technique may offer an opportunity to probe intrinsic reaction kinetics in condensed media without the attendant heat and mass transport effects that are known to influence conventional measurements on bulk samples.

Appendix A

Mathematical Analysis Used for Obtaining Kinetic Parameters. The mathematical methods to be described herein are demonstrated in many good reviews for solid-state reaction kinetics studies. In this study we followed the nomenclature used by Vyazovkin and Wight.¹⁵

Most condensed-phase reactions studied by traditional thermal analyses have been described using the following equation

$$\frac{d\alpha}{dt} = k(T)f(\alpha) \quad (\text{A1})$$

where α is the extent of conversion, $\alpha \equiv (w_0 - w)/(w_0 - w_f)$, w is the sample mass, and the subscripts 0 and f represent the initial and final states of the reaction, respectively. $k(T)$ is the reaction rate constant and temperature-dependent, and $f(\alpha)$ is a mathematical representation of the reaction model. We assumed a single-step first-order reaction for thermal decomposition of metal nitrates throughout the study, in which case $f(\alpha)$ is equal to $1 - \alpha$.

Equation A1 can be written in an integrated form as

$$g(\alpha) \equiv \int_0^\alpha \frac{d\alpha'}{f(\alpha')} = \int_0^t k(T)dt' \quad (\text{A2})$$

where t corresponds to the reaction time which gives the extent of conversion of α . $g(\alpha)$ is equal to $-\ln(1 - \alpha)$ under the first-order reaction assumption. For the SPMS experiment, we assume an isothermal reaction, and thus $k(T)$ is constant with respect to the time. For our analysis, a plug-flow tube reactor model was used. Thus, the reaction duration time t was estimated by dividing the reaction zone volume by the volume flow rate, which was 1.0 L/min measured at room temperature, and was on the order of a second at room temperature. At higher temperatures, the volume flow rate change was estimated assuming the ideal gas law, and the reaction duration was

adjusted for analysis. By applying the Arrhenius relationship for $k(T)$, eq A2 yields

$$\ln(g(\alpha)/t) = \ln k(T) = \ln A - \frac{E}{RT} \quad (\text{A3})$$

Therefore, by making measurements at various temperatures and determining corresponding extents of conversion, the activation energy and preexponential factor are obtained from an Arrhenius plot.

In the case of TGA, the nonisothermal method was used in this study, and eq (A1) is transformed to

$$\frac{d\alpha}{dT} = \frac{k(T)}{\beta} f(\alpha) \quad (\text{A4})$$

with an assumption that the term $d\alpha/dt$ can be expressed as the product of $d\alpha/dT$ and dT/dt , and defining a constant β be equal to dT/dt (the heating rate). We used this transformation which has been widely used in kinetics studies with conventional dynamic thermal techniques, although the method has (as well as other methods) been the subject of criticism. For details, see ref 15. The integral form of eq A4 is generally preferred to eq A4 itself because $d\alpha/dT$ usually suffers from measurement noise, and is given as

$$g(\alpha) = \frac{A}{\beta} \int_{T_0}^T \exp(-E/RT') dT' = \frac{A}{\beta} I(E, T) \quad (\text{A5})$$

where $I(E, T)$ is the temperature integral of the rate constant without the preexponential factor, which does not have an analytical solution. A number of approximation methods for evaluating $I(E, T)$ have been proposed, and Coats and Redfern suggested an asymptotic expansion of the integral term for the case of $2RT/E \ll 1$, which converts eq A5 to

$$\ln[g(\alpha)/T^2] = \ln \left[\frac{AR}{\beta E} \left(1 - \frac{2RT^*}{E} \right) \right] - \frac{E}{RT} \quad (\text{A6})$$

where T^* is the mean experimental temperature.¹⁴ Equation A6 would result in determination of E and A if various combinations of $g(\alpha)$ and T from a single run of TGA were given to eq A6; however, the Arrhenius parameters thus obtained are known to be highly dependent on the reaction model used (i.e., form of $g(\alpha)$),¹⁵ which sometimes might be attributed to the "kinetic compensation" effect, i.e., a strong mutual correlation between E and A .³ Instead, we used the iso-conversional method, which does not choose a specific reaction model in using eq A6. That is, if one can determine the temperatures that correspond to a certain α from multiple measurements with different heating rates, the following equation, which derived from eq A6, can be used to determine the activation energy

$$\ln \frac{\beta_i}{T_{\alpha,i}^2} = \text{constant} - \frac{E_\alpha}{RT_{\alpha,i}} \quad (\text{A7})$$

by plotting $\ln [\beta_i/T_{\alpha,i}^2]$ against $1/T_{\alpha,i}$ where the subscript i represents a TG run at a certain heating rate.^{15,16}

Acknowledgment. Primary support for this work came from the DURINT Army Center for NanoEnergetics Research (Dr. D. Mann-program manager). The SMPS was constructed from an National Science Foundation equipment grant (Dr. Mike Roco-program manager).

References and Notes

- (1) Friedlander, S. K. *Smoke, Dust, and Haze*, 2nd ed.; Oxford University Press: New York, 2001.
- (2) Kudas, T.; Hampden-Smith, M. *Aerosol Processing of Materials*; Wiley-VCH: New York, 1999.
- (3) Ortega, A. *Int. J. Chem. Kinetics* **2001**, *343*, 1.
- (4) Anderson, H. *Thermochim. Acta* **1992**, *33*, 87.
- (5) Reents, W. D.; Ge, Z. *Aerosol Sci. Technol.* **2000**, *33*, 122.
- (6) Reents, W. D.; Schabel, M. J. *Anal. Chem.* **2001**, *73*, 5403.
- (7) Reents, W. D.; Downey, S. W.; Emerson, A. B.; Majsce, A. M.; Muller, A. J.; Siconolfi, D. J.; Sinclair, J. D.; Swanson, A. G. *Aerosol Sci. Technol.* **1995**, *23*, 263.
- (8) Kane, D. B.; Oktem, B.; Johnston, M. V. *Aerosol Sci. Technol.* **2001**, *34*, 520.
- (9) Liu, P.; Zeimann, P. J.; Kittelson, D. B.; McMurry, P. H. *Aerosol Sci. Technol.* **1995**, *22*, 293.
- (10) Liu, P.; Zeimann, P. J.; Kittelson, D. B.; McMurry, P. H. *Aerosol Sci. Technol.* **1995**, *22*, 314.
- (11) Higgins, K. J.; Jung, H.; Kittelson, D. B.; Roberts, J. T.; Zachariah, M. R. *J. Phys. Chem. A* **2001**, *106*, 96.
- (12) *CRC Handbook of Chemistry and Physics*, 77th ed.; CRC Press: Boca Raton, FL, 1996.
- (13) Ettarh, C.; Galwey, A. K. *Thermochim. Acta* **1996**, *288*, 203.
- (14) Coats, A. W.; Redfern, J. P. *Nature* **1964**, *201*, 68.
- (15) Vyazovkin, S.; Wight, C. A. *Int. Rev. Phys. Chem.* **1998**, *17*, 407.
- (16) Brown, M. E. *Introduction to Thermal Analysis Techniques and Applications*; Chapman and Hall: London, 1988.
- (17) Machlin, E. S. *Thermodynamics and Kinetics Relevant to Materials Science*; Giro Press: New York 1991.